SC-MEB: spatial clustering with hidden Markov random field using empirical Bayes

Yi Yang[1,†], Xingjie Shi[2,†], Qiuzhong Zhou[3], Mai Chan Lau[4], Lei Sun[3], Joe Yeong[4,5 *], and Jin Liu[1,*]

[1]Program in Health Services & Systems Research, Duke-NUS Medical School, 8 College Road, 169857, Singapore

[2]Academy of Statistics and Interdisciplinary Sciences, East China Normal University, 3663 Zhongshan North Road, 200062, Shanghai, China

[3]Program in Cardiovascular and Metabolic Disorders, Duke-NUS Medical School, 8 College Road, 169857, Singapore

[4]Institute of Molecular and Cell Biology (IMCB), Agency of Science, Technology and Research (A*STAR), Street, 138673, Singaore

[5]Department of Anatomical Pathology, Singapore General Hospital, 20 College Road, 169856, Singaore

Abstract

Spatial transcriptomics has been emerging as a powerful technique for resolving gene expression profiles while retaining tissue spatial information. These spatially resolved transcriptomics make it feasible to examine the complex multicellular systems of different microenvironments. To answer scientific questions with spatial transcriptomics and expand our understanding of how cell types and states are regulated by microenvironment, the first step is to identify cell clusters by integrating the available spatial information. Here, we introduce SC-MEB, an empirical Bayes approach for spatial clustering analysis using a hidden Markov random field. We have also derived an efficient expectation-maximization algorithm based on an iterative conditional mode for SC-MEB. In contrast to BayesSpace, a recently developed method, SC-MEB is not only computationally efficient and scalable to large sample sizes but is also capable of choosing the smoothness parameter and the number of clusters. We perform comprehensive simulation studies to demonstrate the superiority of SC-MEB over some

existing methods. We apply SC-MEB to analyze the spatial transcriptome of human dorsolateral prefrontal cortex tissues. Our analysis results showed that SC-MEB can achieve a similar clustering performance to BayesSpace, which uses the true number of clusters and a fixed smoothness parameter. We then employed SC-MEB to analyze a colon dataset from a patient with colorectal cancer (CRC) and COVID-19, and further performed differential expression analysis to identify signature genes related to the clustering results. The heatmap of identified signature genes showed that the clusters identified using SC-MEB were more separable than those obtained with BayesSpace. Using pathway analysis, we identified three immune-related clusters, and in a further comparison, found the mean expression of COVID-19 signature genes was greater in immune than non-immune regions of colon tissue. SC-MEB provides a valuable computational tool for investigating the structural organizations of tissues from spatial transcriptomic data.

Keywords: spatial transcriptomics, cell phenotype, empirical Bayes, hidden Markov random field, expectation-maximization algorithm

1 Introduction

Recent advances in spatial transcriptomics (ST) have allowed researchers to simultaneously measure transcriptome-wide gene expression at near single-cell resolution while the spatial information for each measurement is retained [Burgess, 2019]. These spatially resolved transcriptomics have deepened our understanding of how cell types and states are regulated by tissues microenvironment, e.g., of the human brain [Maynard et al., 2021], mouse brain [Shah et al., 2016, Alon et al., 2021], and mouse embryo [Lohoff et al., 2020], among others. The technologies used for resolving spatial gene expression can largely be classified as either imaging-based or next-generation-sequencing-based methods [Waylen et al., 2020]. Imaging-based methods, which were developed to study spatial complexity, are based on fluorescent in situ hybridization (FISH) and include smFISH [Lyubimova et al., 2013], seqFISH [Eng et al., 2017], and MERFISH [Xia et al., 2019]. Although FISH-based methods are capable of capturing both RNA quantity and position, they are limited by their throughput scalability and accuracy in measuring gene expression levels. However, multiple next-generation-sequencing-based methods have been developed to facilitate high-throughput analysis, including Geo-seq [Chen et al., 2017], Slide-seq [Rodriques et al., 2019] and, more recently, the commercial 10x Genomics Visium system [Ståhl et al., 2016]. Emerging ST technologies offer new opportunities to investigate the spatial patterns of gene expression for many applications, such as cell type identification, tissue exploration, and differential expression analysis. Among these applications, gene clustering is the first problem that needs to be addressed.

Similar to single-cell RNA-seq data, ST data contains excessive amounts of zeros or "drop-outs" [Qiu, 2020]. Recently, many academics have argued that drop-outs are mostly due to biological variation, such as cell-type heterogeneity, rather than technical shortcomings [Svensson, 2020]. Kim et al. Kim et al. [2020] suggested that clustering analysis should be performed before imputing or normalizing the data. To overcome the curse of dimensionality due to high-throughput spatial gene expression, clustering is often preceded by standard dimension reduction procedures, e.g., principal component analysis (PCA), t-distributed stochastic neighbor embedding [Van der Maaten and Hinton, 2008], and uniform manifold approximation and projection [McInnes et al., 2018].

In ST datasets, the majority of existing clustering methods, e.g., k-means [Kriegel et al., 2017] and Gaussian mixture models (GMM) [Bishop, 2006], do not consider the available spatial information. To allow additional spatial information to be incorporated into ST datasets, several methods have been recently developed, including the hidden Markov random field model implemented in the *Giotto* package [Zhu et al., 2018, Dries et al., 2019] and a fully Bayesian model with a Markov random field (MRF), BayesSpace [Zhao et al., 2021]. Given the spatial coordinates for each transcriptome-profiled spot, spatial clustering methods achieve better classification accuracy. For example, Zhao et al. [2021] showed that BayesSpace improved the resolution and achieved better classification accuracy for manually annotated human brain samples. However, these methods have certain limitations. First, BayesSpace is a fully Bayesian method based on Markov chain Monte Carlo; therefore, it is not computationally scalable for ST data with high resolution. Second, smoothness is an essential parameter of MRF-based methods and largely determines the proximity of the neighboring spots [Tolpekin and Stein, 2009]. BayesSpace takes this smoothness parameter as fixed and, thus, cannot choose the optimal value that best fits a given dataset. Third, without optimizing the smoothness parameter, one cannot apply any model selection methods to obtain the optimal number of clusters. In practice, the number of clusters in ST datasets is usually unknown before the follow-up analysis, and the preferred method would be to automatically choose the number of clusters.

To address these limitations, we propose a method of Spatial Clustering using the hidden Markov random field based on Empirical Bayes (SC-MEB) to model a low-dimensional representation of a gene expression matrix that incorporates the spatial coordinates for each measurement. In contrast to existing methods [Dries et al., 2019, Zhao et al., 2021], SC-MEB is not only computationally efficient and scalable to larger sample sizes but also accommodates adjustments to the smoothness parameter and the number of clusters. We derived an efficient expectation-maximization (EM) algorithm based on an iterative conditional mode (ICM) and further selected the number of clusters for SC-MEB based on the Bayesian information criterion (BIC) [Claeskens et al., 2008]. We demonstrated the effec-

tiveness of SC-MEB over existing methods through comprehensive simulation studies. We then applied SC-MEB to the clustering analysis of two ST datasets. Using ST data from human dorsolateral prefrontal cortex tissues that were manually annotated, we show the improved clustering performance of SC-MEB spatial clustering methods. The performance of SC-MEB was comparable with that of BayesSpace, even though the latter uses the "true" number of clusters and a prespecified, fine-tuned smoothness parameter. We further applied SC-MEB and alternative methods to analyze ST data of a colon tissue from a patient with colorectal cancer (CRC) and COVID-19. We performed follow-up differential expressions analysis using the clustering results from SC-MEB and BayesSpace, and the heatmap of identified signature genes showed that SC-MEB clustering results were more reasonable and interpretable. Using pathway analysis, we identified three immune-related clusters, and the mean expression of COVID-19 signature genes were further compared between immune and non-immune regions of a colon sample.

2 Materials and Methods

2.1 Problem Formulation

The SC-MEB consists of three major stages (Fig. 1A). First, PCA is conducted on the log-normalized expression of the highly variable genes to obtain the top principal components (PCs) (Fig. 1B). Next, spatial clustering is performed using PCs for each spot. Finally, downstream analyses, such as differential expression analysis, can be performed to obtain signature genes for each cluster (Fig. 1D).

Our spatial clustering method builds on a two-level hierarchical probabilistic model (Fig. 1C). Briefly, for spot i, the first level specifies the conditional probability of the low-dimensional representation (e.g., top PCs) of its gene expression y_i given an unknown label $x_i \in \{1, \ldots, K\}$, where K is the number of clusters. In SC-MEB, we assume that given the labels for each spot, a d-dimensional representation y_i is mutually independent among all spots, and its distribution within a given cluster k can be written as

$$p(y \mid x, \theta) = \prod_{i \in \mathcal{S}} \mathcal{N}(y_i | x_i = k, \mu_k, \Sigma_k), \tag{1}$$

where $\theta = \{\mu_k, \Sigma_k : k = 1, \ldots, K\}$, and μ_k and Σ_k denote the mean and covariance matrix for cluster k, respectively.

The second level of SC-MEB depicts the prior probability of the hidden labels, and an MRF prior is implemented to encourage smoothness among spots. In other words, spots of the same cluster can be in close proximity. As spots in Visium are primarily arranged

on hexagonal lattices, the neighborhood of each spot is defined by applying a proximity threshold. To promote smoothness within spot neighborhoods, Potts energy $U(x)$ [Zhang et al., 2001] is employed, which ranks all possible configurations proportionally to a positive parameter β. Thus, the Potts model promotes spatial smoothness by penalizing cases in which neighboring spots are assigned to different cluster labels. The hidden random field x is assumed to be

$$P(x) = \frac{1}{Z_\beta} \exp\{-U(x)\}, \tag{2}$$

where $U(x) = \sum_{i,i' \in \mathcal{N}_i} \beta[1 - \delta(x_i, x_i')]$, δ is the delta function, and Z_β is a normalization constant that does not have a closed form. When all labels on a neighborhood take the same value, meaning that the hidden x is locally smooth, it incurs no neighborhood cost; otherwise, if they are not all the same, a positive cost is incurred, and the amount of cost is controlled by parameter β. Thus, parameter β controls the smoothness in latent labels; the larger the β, the spatially smoother the latent labels. When β is zero, SC-MEB reverts to the method that does not consider spatial information, i.e., GMM. Combining two levels of SC-MEB, (1) and (2), we denote $\phi = (\theta, \beta)$ the parameter space.

As the smoothing parameter β does not have an explicit updated form, SC-MEB adaptively selects β via a grid search strategy. That is, the SC-MEB model is trained with a prefixed β using an efficient ICM-EM scheme [Cuadra et al., 2005] that incorporates a pseudo-likelihood maximization step, as in the ICM method of Besag [1974]. The optimal β is the value that maximizes the marginal log-likelihood. In a similar way, the marginal log-likelihood can be evaluated for a sequence of K. Then, BIC [Forbes and Peyrard, 2002] is applied to choose the optimal number of clusters in a data-driven manner (Fig. 1D). Please refer to Supplementary for more details about the BIC used in this case.

2.2 ICM-EM Algorithm

The parameter is estimated through an iterative-conditional-mode-based expectation-maximization (ICM-EM) algorithm [Cuadra et al., 2005]. Here, we assume (K, β) is known.

In the ICM step, the estimate of x is obtained by maximizing its posterior with respect to x_i coordinately:

$$P(x \mid y) = P(x_i, x_{\mathcal{S}-\{i\}} \mid y) = P(x_i \mid y, x_{\mathcal{S}-\{i\}}) P(x_{\mathcal{S}-\{i\}} \mid y),$$

where $i = 1, \ldots, n$, until converge [Besag, 1986]. Given initial values of x, θ, and observed y, we have the updated equation:

$$\hat{x}_i = \min_{x_i} U(\hat{x}_1, \ldots, x_i, \ldots, \hat{x}_n), \tag{3}$$

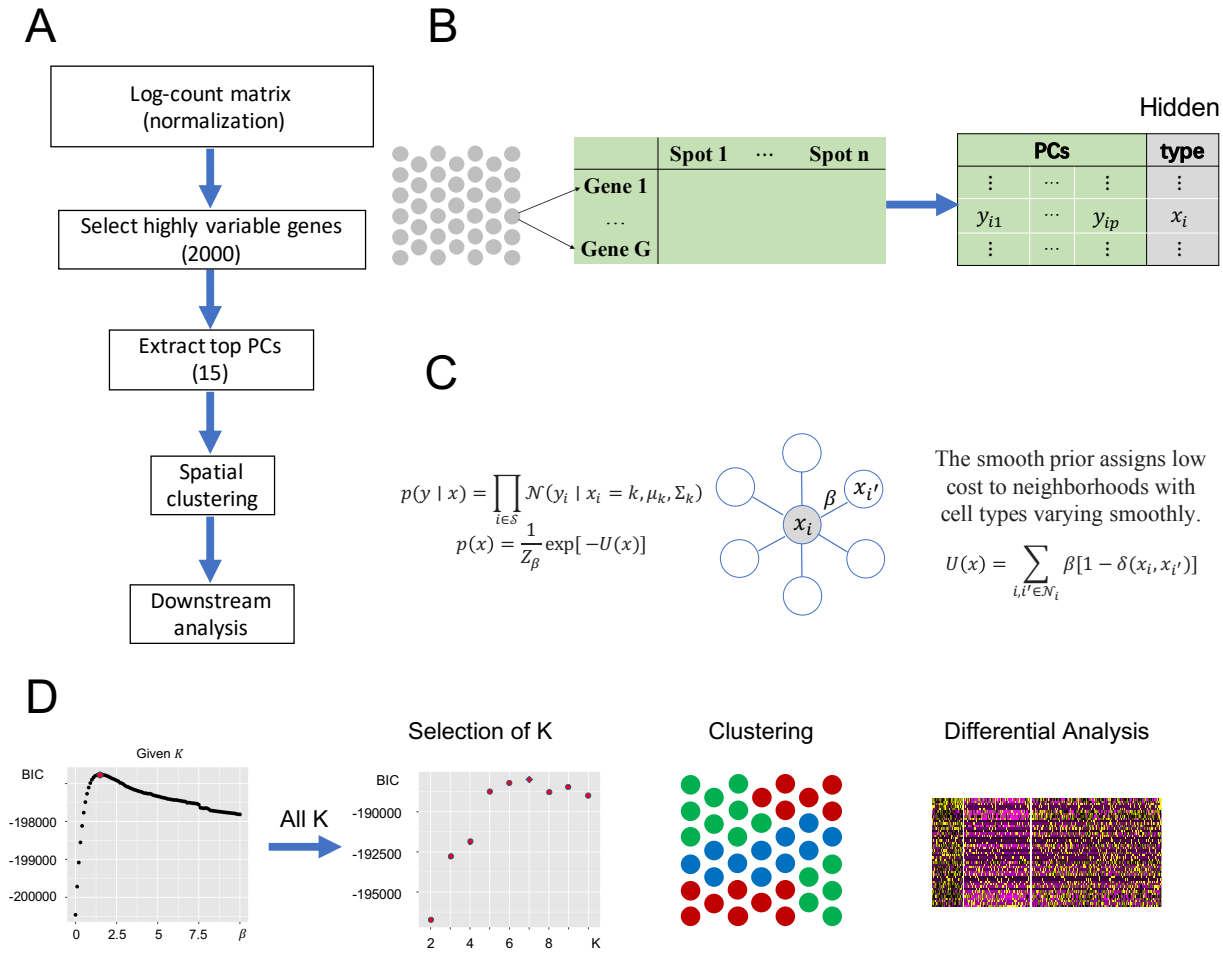

Figure 1: SC-MEB workflow. **A.** SC-MEB workflow. **B.** Data preprocessing. **C.** The hidden MRF model. For the Visium dataset, we used 6 neighborhoods for each spot. **D.** The outputs of SC-MEB.

where

$$U(x) = \{\frac{1}{2}(y_i - \mu_{x_i})^\top \Sigma_{x_i}^{-1}(y_i - \mu_{x_i}) + \frac{1}{2}\log|\Sigma_{x_i}| + \beta \sum_{i' \in \mathcal{N}_i} [1 - \delta(x_i, x_{i'})]\}.$$

In the expectation (E) step, instead of using the original complete likelihood, which is difficult to evaluate, the following pseudo-likelihood is used:

$$\begin{aligned}\tilde{p}(y, x; \theta) &= p(y|x;\theta)\tilde{p}(x;\theta) \\ &= \prod_i p(y_i \mid x_i;\theta) \prod p(x_i|x_{\mathcal{N}_i};\theta)\end{aligned}$$

$$= \prod_i [p(y_i \mid x_i; \theta) p(x_i | x_{\mathcal{N}_i}; \theta)]$$
$$= \prod_i p(y_i, x_i \mid x_{\mathcal{N}_i}; \theta).$$

With the optimal conditional distribution of x (details in Supplementary), we have

$$Q(\theta) = \sum_i \sum_k \gamma_{ik} \left[\log p(y_i \mid x_i = k; \theta) + \log p(x_i = k \mid x_{\mathcal{N}_i}; \theta) \right],$$

where γ_{ik} is the responsibility that component k has for explaining the observation y_i, which is defined as follows:

$$\gamma_{ik} = \frac{P(y_i \mid x_i = k) P(x_i = k \mid X_{\mathcal{N}_i} = \hat{x}_{\mathcal{N}_i})}{\sum_{k'} P(y_i \mid x_i = k') P(X_i = k' \mid X_{\mathcal{N}_i} = \hat{x}_{\mathcal{N}_i})}. \tag{4}$$

By taking partial derivatives of $Q(\theta)$ with respect to the parameters and setting them to zero, we obtain the updated equations for the maximization (M) step:

$$\mu_k = \frac{1}{N_k} \sum_{i=1}^{n} \gamma_{ik} y_i, \tag{5}$$

$$\Sigma_k = \frac{1}{N_k} \sum_{i=1}^{n} \gamma_{ik} (y_i - \mu_k)(y_i - \mu_k)^\top. \tag{6}$$

where $N_k = \sum_{i=1}^{n} \gamma_{ik}$.

The ICM-EM algorithm iterates the ICM step and M step until convergence. Further details on the ICM-EM algorithm are provided in the Supplementary Material.

2.3 Methods for comparison

We conducted comprehensive simulations and real data analysis to gauge the performance of different methods for clustering a low-dimensional representation of a gene expression matrix, including both non-spatial and spatial clustering methods.

In detail, we considered the following non-spatial clustering methods: (i) k-means implemented in the R package *stats*, available at CRAN; (ii) GMM implemented in the R package *mclust*, available at CRAN; (iii) Louvain implemented in the R package *igraph*, available at https://igraph.org/r/. In addition, we compared the clustering performance of spatial methods: (i) SC-MEB implemented in the R package *SC.MEB*, available at https://github.com/Shufeyangyi2015310117/SC.MEB; (ii) BayesSpace implemented in the R package *BayesSpace*, available at Bioconductor; (iii) HMRF implemented in the *Giotto* package, available at http://spatialgiotto.rc.fas.harvard.edu/.

2.4 Preprocessing of ST datasets

The Visium spatial transcriptomics [Zhao et al., 2021] data were aligned and quantified using Space Ranger downloaded from 10x Genomics official website against the GRCh38 human reference genome also from 10x Genomics official website. For all datasets, we applied log-transformation and normalization of the raw count matrix using library size [Lun et al., 2016, McCarthy et al., 2017]. Then, we performed PCA on the 2,000 most highly variable genes. In the clustering analysis, we chose the top 15 PCs from the study datasets as the input for SC-MEB as well as for the alternative methods.

2.5 ST datasets

2.5.1 Human dorsolateral prefrontal cortex (DLPFC)

[Maynard et al., 2021] used recently released ST technology, the 10x Genomics Visium platform, to generate spatial maps of gene expression matrices for the six-layered DLPFC of the adult human brain that are provided in the *spatialLIBD* package. They also provided manual annotations of the layers based on the cytoarchitecture. In their study, they profiled the spatial transcriptomics of human postmortem DLPFC tissue sections from 12 samples, with a median depth of 291 M reads for each sample, corresponding to a mean 3,462 unique molecular indices and a mean 1,734 genes per spot.

2.5.2 Human colon tissue adjacent to colorectal cancer (CRC)

The colon tissue was from a 45-year-old South Asian male who was diagnosed with COVID-19 on April 16, 2020. As previously described [Cheung et al., 2021], the patient had experienced mild upper respiratory tract symptoms throughout the course of the disease. He was confirmed COVID-19-negative after two consecutive nasopharyngeal swabs on and May 9 and 10, 2020, and was discharged from the isolation facility on May 10, 2020. During hospital admission, further investigation involving computed tomography scanning and colonoscopy revealed the presence of a large circumferential malignant mass in the cecum. Histology of the biopsies confirmed that the patient had invasive colorectal cancer stage II T3N0. He underwent laparoscopic right hemicolectomy on May 18, 2020, 9 days after testing negative for COVID-19. He recovered uneventfully and was discharged on May 21, 2020. Using this sample, we profiled the spatial transcriptomics using the 10x Genomics Visium platform. In summary, it has a depth of 143 million reads for a total of 2988 spots within the tissue and a median 492 genes per spot.

2.6 Evaluation metrics

We evaluated the clustering performance by adjusted Rand index (ARI) [Schütze et al., 2008]. The general formula for ARI is as follows

$$\text{ARI} = \frac{(\text{RI} - \text{expected}(\text{RI}))}{(\max(\text{RI}) - \text{expected}(\text{RI}))} \tag{7}$$

where RI is the Rand index [Rand, 1971], and max (RI) and expected (RI) are the maximum value and the expected value of RI, respectively. Assuming that n is the number of spots in an ST dataset. $U = \{u_1, \ldots, u_i, \ldots, u_R\} \in \mathbb{R}^n$ and $V = \{v_1, \ldots, v_j, \ldots, v_C\} \in \mathbb{R}^n$ represent two clustering labels for n spots, where R and C are the corresponding numbers of clusters in U and V, respectively. Denoting n_{ij} as the number of spots belonging to both classes u_i and v_j, and $n_{i\cdot}$ and $n_{\cdot j}$ as the number of spots in classes u_i and v_j, respectively; then ARI (7) is defined as

$$\text{ARI}(U, V) = \frac{\sum_{i,j} \binom{n_{ij}}{2} - \sum_i \binom{n_{i\cdot}}{2} \sum_j \binom{n_{\cdot j}}{2} \Big/ \binom{n}{2}}{\frac{1}{2}\left[\sum_i \binom{n_{i\cdot}}{2} + \sum_j \binom{n_{\cdot j}}{2}\right] - \left[\sum_i \binom{n_{i\cdot}}{2} \sum_j \binom{n_{\cdot j}}{2}\right] \Big/ \binom{n}{2}}. \tag{8}$$

As the expected value of RI for two random partitions does not take a constant value and is concentrated within a small interval, ARI is a corrected version of RI to avoid these drawbacks [Hubert and Arabie, 1985]. Note that ARI lies between -1 and 1 and takes a value of 1 when the two partitions are equal up to a permutation. Obviously, a larger ARI value indicates a higher similarity between two partitions. In the simulation, ARI was used to measure the similarity between the estimated partition and the true one. In the analysis of the DLPFC dataset [Maynard et al., 2021], manual annotations based on additional experiments and computational results were available. ARI was used to measure the similarity between labels from the estimated partition and the manually annotated clusters.

3 Results

3.1 Simulation settings

Using simulations, we compared the clustering performance of SC-MEB and with five other methods, including k-means, GMM, Louvain, BayesSpace, and Giotto. For both k-means and BayesSpace, we considered the true number of clusters K, and its two nearest numbers, $K - 1$ and $K + 1$, as the number of clusters had to be manually specified for these two methods. For all other methods, the number of clusters was selected automatically. The smoothness parameter β of BayesSpace was fixed at 3 by default, while β of SC-MEB was

optimized with a grid search. We compared the clustering performances using ARI for all methods, in which we ran 50 replicates in each setting.

In Example I, the labels for spots were randomly generated. In detail, for a 70×70 squared lattice with 4,900 spatial spots, we generated cluster labels for each spot from the K-states Potts model (as shown in Eqn. (2)) with $\beta \in [1, 1.3]$ using the R package *GiRaF*. The number of neighbors was set to be 4, and the number of true clusters K was set to 3, 5, or 7. We then considered two distributions for low-dimensional PCs: a mixture of Gaussian and a mixture of Student-t distributions. The number of PCs was set to either 10 or 15. The mean μ_k and the covariance matrix Σ_k for each component k are listed in Supplementary Tables S1-S4.

In Example II, labels for spots were obtained from real data analysis. In detail, we used the inferred cluster labels from SC-MEB ($K = 8$) of colon data as the true labels for all 2,988 spots. PCs were randomly generated in the same way as in Example I. The mean μ_k and the covariance matrix Σ_k for each component k are provided in Supplementary Tables S5-S6.

In the above examples, all K components had different covariance matrices. Because BayesSpace adopts a strategy in which all components have a shared covariance, we further conducted additional simulations with equal covariance matrices.

3.2 Performance of SC-MEB in comparison with other methods in simulation studies

In Example I, when PCs were from a mixture of Gaussian distributions, SC-MEB was more powerful than all other methods (Fig. 2A). BayesSpace had a smaller ARI, i.e. poorer concordance between predicted and true clustering assignment, than SC-MEB, even when the true number of clusters was used as input. The inferior performance of BayesSpace was due to its lack of adaptation to the smoothness parameter β. The other methods, Giotto, GMM, k-means, and Louvain, achieved lower ARIs. When PCs were from a mixture of Student t distributions, assumptions of BayesSpace were satisfied. As shown in Fig. 2B, using BayesSpace with the correct number of clusters showed the best performance. Even though SC-MEB was miss-specified in this setting, it still achieved a high ARI that was larger than that of BayesSpace with miss-specificed K and other methods. This demonstrates the robustness of SC-MEB performance when there is miss-specification of distributions. The results from other settings (Supplementary Fig. S1-S2) prompted similar conclusions.

In Example II, the comparative results (Fig. 2C and 2D) were largely consistent with the results obtained in Example I. Specifically, SC-MEB was more powerful than all the other methods. The performance of BayesSpace was the next most powerful, and k-means had the

worst performance. The results obtained from other settings (Supplementary Fig. S5A-S5B, S6A-S6B) led to similar conclusions.

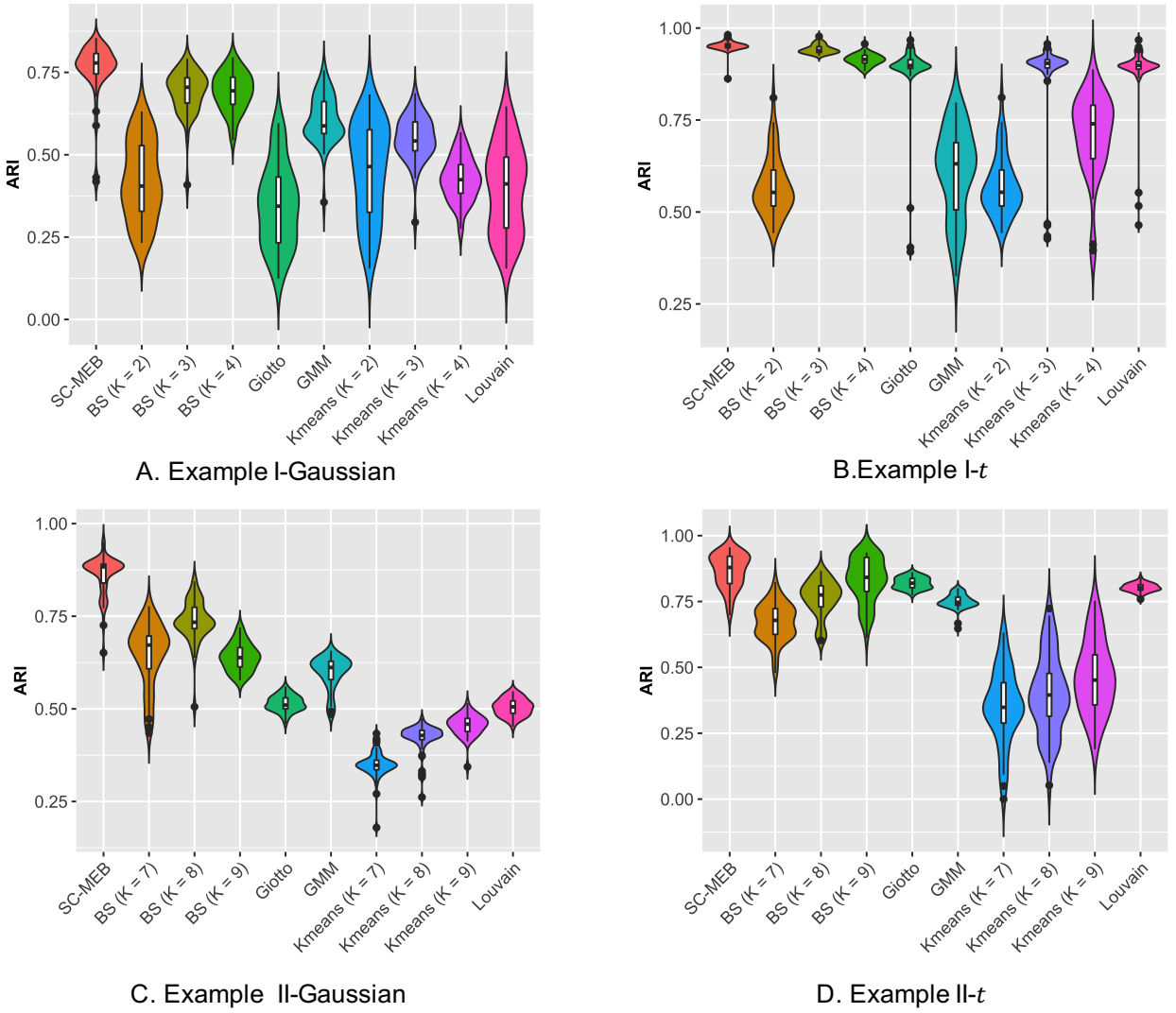

Figure 2: Summary of clustering accuracy of the six methods in the analysis of simulated data. **A.** Example 1, Gaussian: PCs were sampled from a Gaussian mixture model. **B.** Example 1, t: PCs were sampled from a Student t mixture model. **C.** Example 2, Gaussian: PCs were sampled from a Gaussian mixture model. **D.** Example 2, t: PCs were sampled from a Student t mixture model.

Finally, we considered the above two examples under BayesSpace's assumption that all K components share a common covariance. The results are shown in (Supplementary Fig. S3-S4, S5C-D, and S6C-D). As is shown, the ARI of SC-MEB was comparable with that of BayesSpace, and both demonstrated better performance than the other methods.

All simulations were conducted on a computer with a 2.1 GHz Intel Xeon Gold 6230 CPU and 16 GB memory. SC-MEB was computationally more efficient than BayesSpace.

In all simulations, SC-MEB took approximately 8 minutes to complete the analysis for 200 combinatorial values in K and β, while BayesSpace required about 25 minutes for prefixed K and β and up to 600 times more computation time than SC-MEB for fixed combinatorial values of K and β. To better demonstrate the computational efficiency and scalability of SC-MEB, we conducted additional simulations with an increasing sample size n. In Fig. 3, we can see that the computation time of SC-MEB for a fixed number of iterations increased almost linearly with increasing sample size, taking about 12.5 hours to run 50 iterations for a dataset with 100K spots. Thus, SC-MEB can be used to perform clustering analysis for ST datasets with a higher resolution than other methods.

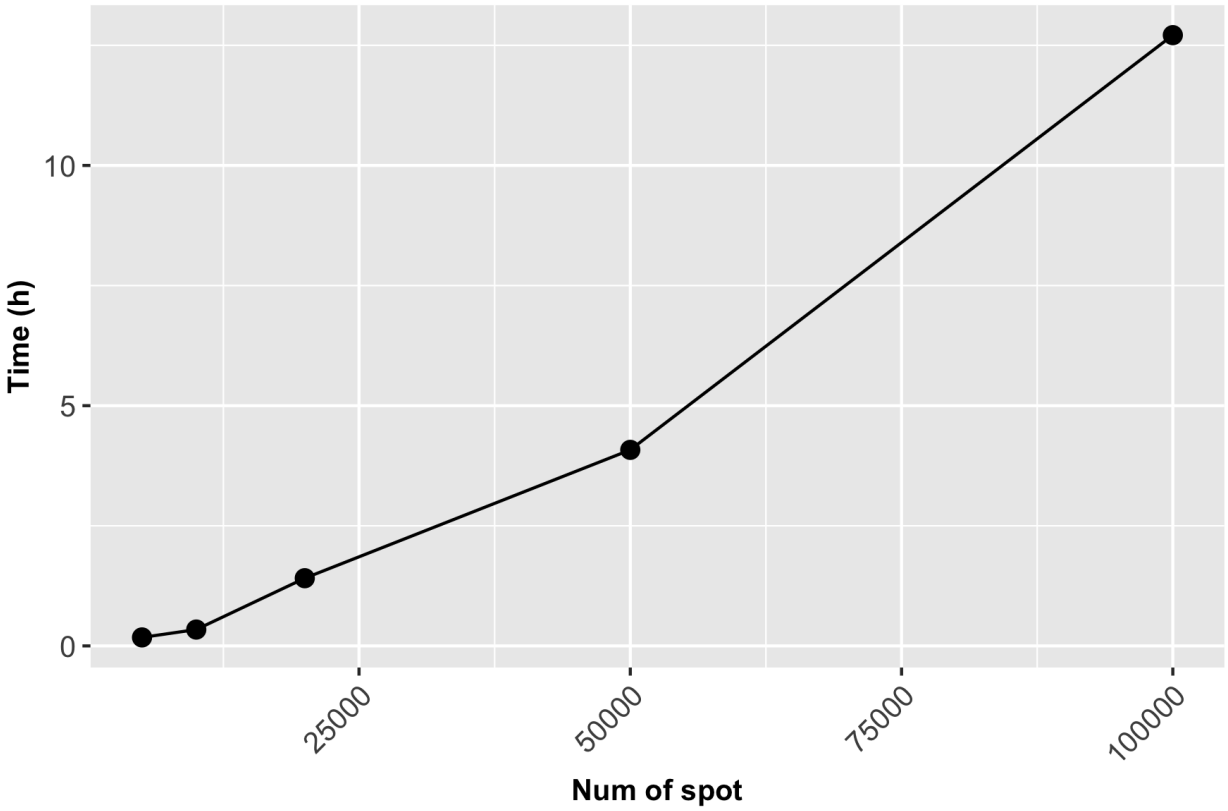

Figure 3: Computation time of SC-MEB increases linearly with sample size. The number of iterations were set to 50 for the different sample sizes.

3.3 Benchmark clustering performance with DLPFC dataset

To evaluate the clustering performance of SC-MEB with real datasets, it was first applied to the DLPFC dataset and the performance compared with that of alternative methods. Specifically, we obtained the top 15 PCs from the 2,000 most highly variable genes in each DLPFC sample and performed clustering analysis with all methods, except k-means. As

Table 1: Clustering accuracy for DLPFC dataset. ARI values were evaluated by comparing manual annotations against cluster labels from SC-MEB and alternative methods for all 12 samples.

ID	SC-MEB	BayesSpace	GMM	Giotto	Louvain
151507	**0.45**	0.33	0.40	0.33	0.32
151508	**0.37**	0.36	0.33	0.33	0.25
151509	**0.45**	0.44	0.29	0.29	0.30
151510	**0.46**	0.43	0.31	0.32	0.28
151669	0.27	**0.41**	0.22	0.15	0.20
151670	0.24	**0.43**	0.19	0.13	0.26
151671	0.34	**0.38**	0.23	0.25	0.36
151672	0.44	**0.77**	0.14	0.27	0.27
151673	0.38	**0.55**	0.29	0.26	0.29
151674	0.33	0.33	0.29	**0.34**	0.33
151675	0.37	**0.41**	0.24	0.28	0.24
151676	**0.34**	0.32	0.26	0.26	0.25

BayesSpace cannot choose the number of clusters K, the K was set to the number of clusters in the manual annotations. All other methods selected the number of clusters automatically.

Table 1 shows the ARI values for 12 DLPFC samples, where the manually annotated layers were taken as the "ground truth". SC-MEB clearly outperformed BayesSpace in the analysis of five samples, and vice versa for the other six samples. In the analysis, BayesSpace took both the "true" number of clusters (from the manual annotations) and the prefixed fine-tuned β as input. In this case, the proposed SC-MEB achieved the similar performance without the prior information. Additionally, SC-MEB achieved the best clustering performance among the methods that can select (K) automatically. Table 2 compares the computational times required for all methods. The computational time of SC-MEB was based on a sequence of values for β and K. For a fixed β and K, the speed of SC-MEB was almost 2,000 times faster than that of BayesSpace. Even though GMM, Giotto, and Louvain were faster than SC-MEB, the clustering performances of these methods less powerful than SC-MEB and BayesSpace (Table 1).

3.4 Spatial clustering of in-house CRC sample

To apply SC-MEB in the analysis of an in-house colon sample from a patient suffeed from CRC and COVID-19, we first obtained the top 15 PCs, as described for the DLPFC dataset. The spatial clustering performed by SC-MEB was compared with that of other methods. Because SC-MEB, Giotto, and Louvain selected eight clusters as the optimal number (K), we also ran BayesSpace with eight clusters. The computational times for SC-MEB, BayesSpace,

Table 2: Comparison of computation times (s) of five methods of DLPFC analysis. Note, that for SC-MEB, we used a K sequence from 2 to 10 and a beta sequence from 0 to 4 with equal space (0.2).

ID	SC-MEB	BayesSpace	GMM	Giotto	Louvain
151507	234.63	7015.95	46.16	21.68	2.86
151508	230.33	5471.57	36.26	41.26	6.97
151509	230.04	4660.43	53.22	33.95	6.00
151510	236.77	4288.56	39.50	42.10	7.57
151669	205.63	5840.10	20.96	16.01	3.49
151670	190.27	4917.43	37.94	26.49	5.26
151671	214.03	3889.07	31.01	38.61	8.82
151672	206.11	3793.58	22.44	33.74	5.49
151673	191.48	5984.89	40.20	18.26	1.49
151674	165.63	5344.68	36.82	38.24	3.34
151675	178.01	3863.19	27.90	31.63	4.22
151676	168.54	3609.71	37.44	28.90	3.24

GMM, Giotto, and Louvain were 165.80, 5324.48, 46.26, 19.75, and 0.69 seconds, respectively.

The clustering results obtained using the different methods are shown in Fig. 4. In general, the pattern of clustering assigned by SC-MEB was similar to that of GMM, but the latter retained more noisy spots. In addition, the results from SC-MEB and BayesSpace had stronger spatial patterns than those of the other methods.

By checking PanglaoDB [Franzén et al., 2019] for signature genes identified via *differential expression (DE) analysis* and with the help of the H&E staining shown in Fig. 4A, we were able to identify regions of muscle, stroma, epithelial, and immune cells. As shown in Fig. 4B-F, all methods except BayesSpace returned good partitions for the muscle region, which were visually verified with the H&E staining (Fig. 4A). The epithelial regions identified by BayesSpace were much smaller than those identified by SC-MEB, in which a large proportion of the epithelial regions in Fig. 4B-C were classified as stromal regions (stroma 2) by BayesSpace. The immune regions identified by BayesSpace were larger at the 9 and 12 o'clock positions but smaller at the 6 o'clock position in Fig. 4C than those identified by SC-MEB (Fig. 4B) and GMM (Fig. 4F). Strikingly, a large proportion of the regions identified as stroma 1 by both SC-MEB and GMM were classified as stroma 2 by BayesSpace. Even though stroma 1 and stroma 2 are both stromal regions, one can observe clear differences in the normalized expression of signature genes for these two clusters (Fig. 5). These observations illustrate the possible over-smoothing behavior of BayesSpace, while SC-MEB was able to recover the fine structure of tissues.

3.4.1 Differential expression analysis of the identified clusters

As true labels for all spots were not available for the colon dataset, we could not quantitatively evaluate the clustering performance. For the clustering results of SC-MEB and BayesSpace, we further performed DE analysis comparing an identified cluster with all others using the *BPSC* package [Vu et al., 2016] for log-normalized expression. Using the partition results from SC-MEB, we identified 190, 154, 134, 102, 98, 89, 137, and 99 genes that were differentially expressed for stroma 1 and 2; muscle; epithelial 1 and 2; and immune 1, 2, and 3, respectively, with a false discovery rate of < 0.05. The details of all differentially expressed genes identified by SC-MEB and BayesSpace are provided in Supplementary Tables S7 and S8. We further restricted the number of signature genes by choosing those with log-fold changes larger than 0.5. Finally, we obtained a total of 78 and 57 signature genes for SC-MEB and BayesSpace, respectively.

Fig. 5 shows the heatmap of normalized expression for the signature genes identified in the DE analysis by SC-MEB (Fig. 5A) and BayesSpace (Fig. 5B), respectively. Clearly, with BayesSpace, the normalized expression of signature genes in stroma 2 could be further divided into two sub-clusters, and the expression pattern in the second sub-cluster was very similar to that of stroma 1. This misclassification is also apparent when comparing Fig. 4B and Fig. 4C, as a large proportion of the regions identified as stroma 1 by SC-MEB were identified as stroma 2 by BayesSpace. The findings obtained using SC-MEB demonstrated that stroma 1 and stroma 2 clusters, epithelial clusters, and immune clusters were arranged in layers that are morphologically supported by the anatomical architecture of colonic tissue [Mills, 2019]: (from lumen to serosa) mucosal epithelium; lamina propria (in which immune cells are abundant, and the isolated lymphoid nodules present in this tissue extend into the submucosal layer); submucosal layer, the stromal layer with abundant connective tissue; and lastly muscularis externa, which is represented by the muscle layer.

3.4.2 Pathway analysis of the signature genes identified in the DE analysis

We further conducted pathway analysis using gene ontology [Consortium, 2021] for the signature genes from each cluster identified by SC-MEB. Supplementary Table S9 shows the top four pathways in each cluster. For the regions identified as muscle, muscle system development and muscle contraction were the two most significant pathways. For the three identified immune clusters, the most significant pathways included humoral immune response and antimicrobial humoral response. For stroma 1 and 2 clusters, extracellular structure organization, extracellular matrix organization, and external encapsulating structure organization were among the most significant pathways. We also found similar patterns in the heatmap for the normalized expression of signature genes (Fig. 5) between stroma 1 and 2

clusters, among the three immune clusters, and between epithelial clusters 1 and 2. There was high cosine similarity between the two stromal clusters (0.97), as well as among the immune clusters (see Supplementary Table S10). We ultimately compared the mean expression of COVID-19 signature genes [Lee et al., 2020] in the immune and non-immune regions identified by SC-MEB (Fig. 6), and it was clear that COVID-19 signature genes were more highly expressed in the immune regions than the non-immune regions of the colorectal tumor sample.

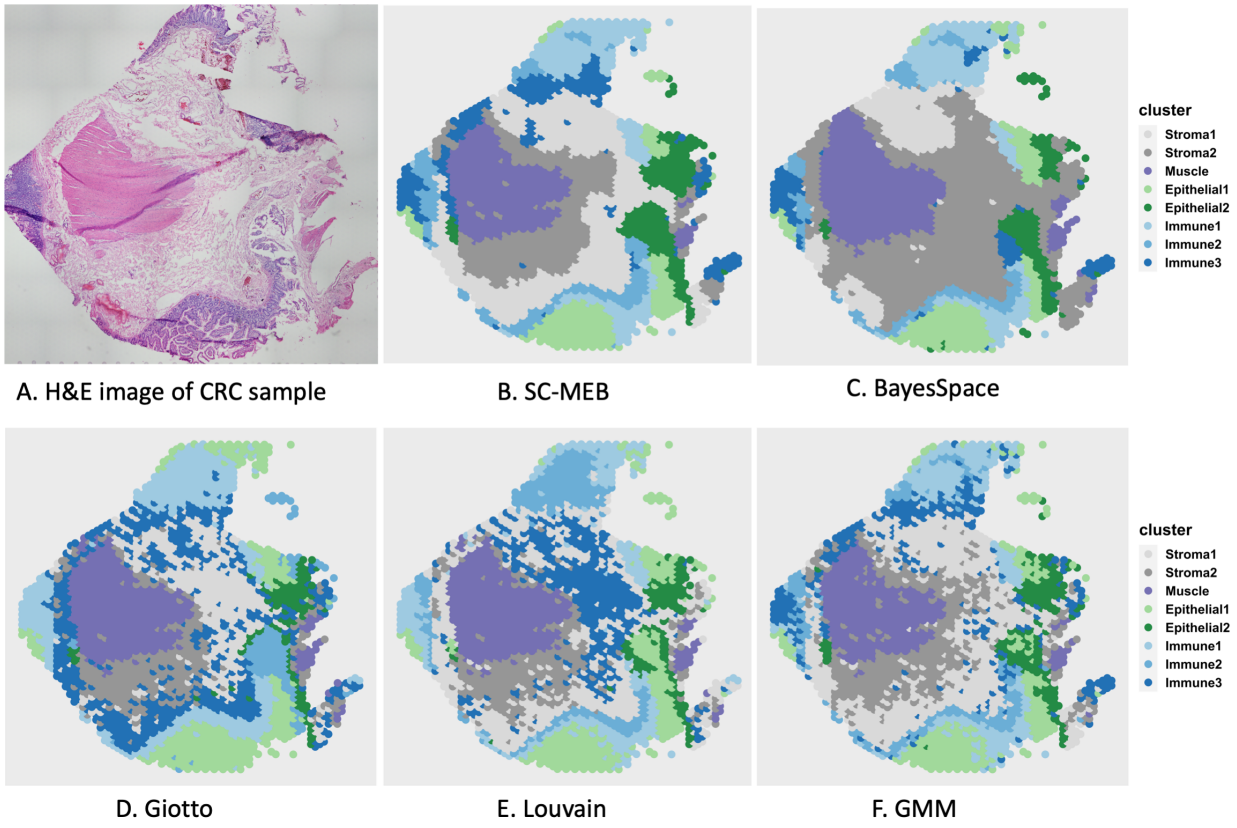

Figure 4: Clustering results for a colon sample. (A) Original H&E-stained tissue image for the colon sample. (B-F) Heatmaps for clustering assignments in the colon sample using the proposed SC-MEB, BayesSpace, Giotto, Louvain, and GMM, respectively. The eight clusters identified included two stromal regions, a muscle region, two epithelial-cell regions, and three immune-cell regions.

4 Competing interests

The authors have no competing interests.

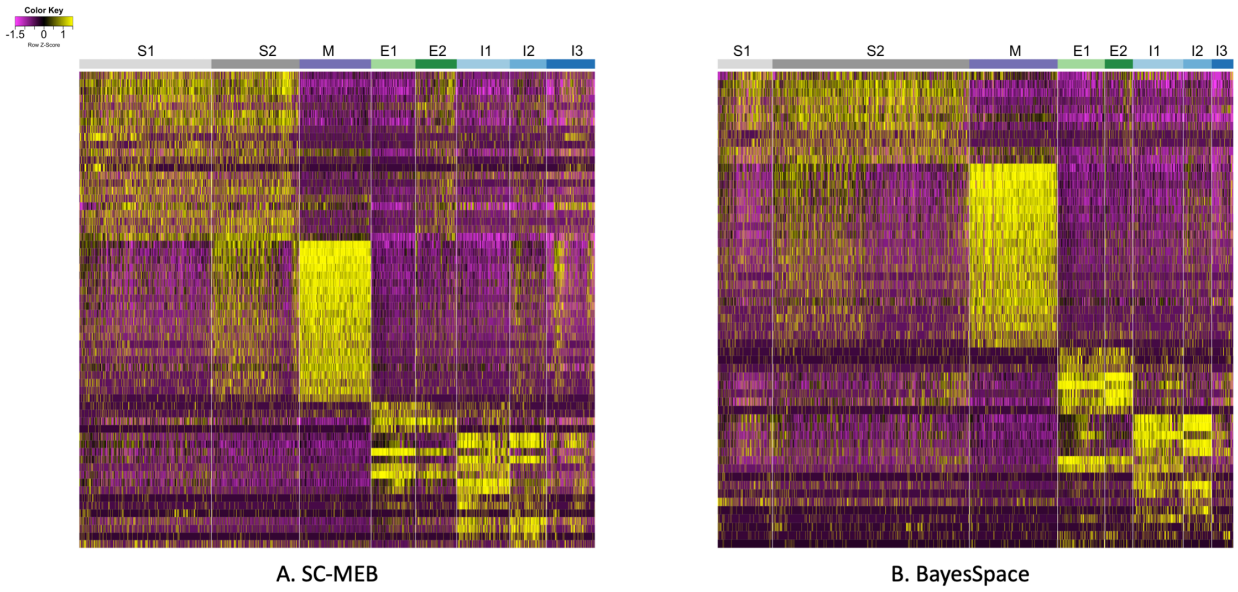

Figure 5: Heatmaps of normalized expression of signature genes identified in the differential expression analysis based on two clustering analysis methods: (A) SC-MEB and (B) BayesSpace. In both subfigures, S1 and S2 represent Stroma 1 and 2, respectively; M is Muscle; E1 and E2 are Epithelial 1 and 2, respectively; and I1, I2, and I3 are Immune 1, 2, and 3, respectively.

5 Author contributions statement

J.L. and J.Y. initiated and designed the study, X.S. and Y.Y. implemented the model and performed simulation studies and benchmarking evaluation, X.S. and J.L. wrote the manuscript, and all authors edited and revised the manuscript.

6 Acknowledgments

This work was supported by grant R-913-200-098-263 from the Duke-NUS Medical School, AcRF Tier 2 (MOE2018-T2-1-046 and MOE2018-T2-2-006) from the Ministry of Education, Singapore, grants (NSF: # 1636933 and # 1920920) from the National Science Foundation of China.

References

S. Alon, D. R. Goodwin, A. Sinha, A. T. Wassie, F. Chen, E. R. Daugharthy, Y. Bando, A. Kajita, A. G. Xue, K. Marrett, et al. Expansion sequencing: Spatially precise in situ transcriptomics in intact biological systems. *Science*, 371(6528), 2021.

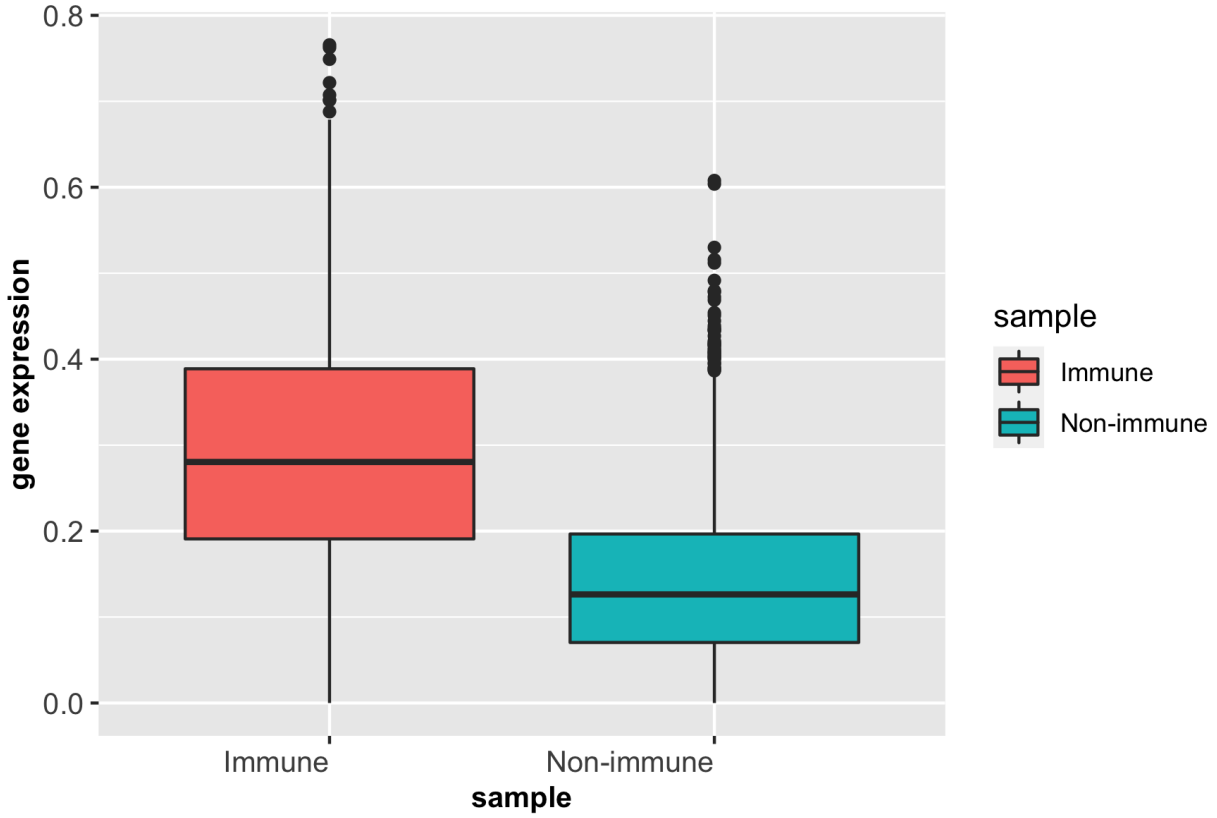

Figure 6: Boxplots of mean expression of COVID-19 signature genes in immune and non-immune regions.

J. Besag. Spatial interaction and the statistical analysis of lattice systems. *Journal of the Royal Statistical Society: Series B (Methodological)*, 36(2):192–225, 1974.

J. Besag. On the statistical analysis of dirty pictures. *Journal of the Royal Statistical Society: Series B (Methodological)*, 48(3):259–279, 1986.

C. M. Bishop. *Pattern recognition and machine learning*. springer, 2006.

D. J. Burgess. Spatial transcriptomics coming of age. *Nature Reviews Genetics*, 20(6): 317–317, 2019.

J. Chen, S. Suo, P. P. Tam, J.-D. J. Han, G. Peng, and N. Jing. Spatial transcriptomic analysis of cryosectioned tissue samples with geo-seq. *Nature protocols*, 12(3):566–580, 2017.

C. C. L. Cheung, D. Goh, X. Lim, T. Z. Tien, J. C. T. Lim, J. N. Lee, B. Tan, Z. E. A. Tay, W. Y. Wan, E. X. Chen, et al. Residual sars-cov-2 viral antigens detected in gi and hepatic tissues from five recovered patients with covid-19. *Gut*, 2021.

G. Claeskens, N. L. Hjort, et al. Model selection and model averaging. *Cambridge Books*, 2008.

T. G. O. Consortium. The gene ontology resource: enriching a gold mine. *Nucleic Acids Research*, 49(D1):D325–D334, 2021.

M. B. Cuadra, L. Cammoun, T. Butz, O. Cuisenaire, and J.-P. Thiran. Comparison and validation of tissue modelization and statistical classification methods in t1-weighted mr brain images. *IEEE transactions on medical imaging*, 24(12):1548–1565, 2005.

R. Dries, Q. Zhu, C.-H. L. Eng, A. Sarkar, F. Bao, R. E. George, N. Pierson, L. Cai, and G.-C. Yuan. Giotto, a pipeline for integrative analysis and visualization of single-cell spatial transcriptomic data. *BioRxiv*, page 701680, 2019.

C.-H. L. Eng, S. Shah, J. Thomassie, and L. Cai. Profiling the transcriptome with rna spots. *Nature methods*, 14(12):1153–1155, 2017.

F. Forbes and N. Peyrard. *Hidden Markov Models Selection Criteria based on Mean Field-like approximations*. PhD thesis, INRIA, 2002.

O. Franzén, L.-M. Gan, and J. L. Björkegren. Panglaodb: a web server for exploration of mouse and human single-cell rna sequencing data. *Database*, 2019, 2019.

L. Hubert and P. Arabie. Comparing partitions. *Journal of classification*, 2(1):193–218, 1985.

T. H. Kim, X. Zhou, and M. Chen. Demystifying "drop-outs" in single-cell umi data. *Genome biology*, 21(1):1–19, 2020.

H.-P. Kriegel, E. Schubert, and A. Zimek. The (black) art of runtime evaluation: Are we comparing algorithms or implementations? *Knowledge and Information Systems*, 52(2): 341–378, 2017.

J. S. Lee, S. Park, H. W. Jeong, J. Y. Ahn, S. J. Choi, H. Lee, B. Choi, S. K. Nam, M. Sa, J.-S. Kwon, et al. Immunophenotyping of covid-19 and influenza highlights the role of type i interferons in development of severe covid-19. *Science immunology*, 5(49), 2020.

T. Lohoff, S. Ghazanfar, A. Missarova, N. Koulena, N. Pierson, J. A. Griffiths, E. S. Bardot, C.-H. L. Eng, R. C. Tyser, R. Argelaguet, et al. Highly multiplexed spatially resolved gene expression profiling of mouse organogenesis. *bioRxiv*, 2020.

A. T. Lun, K. Bach, and J. C. Marioni. Pooling across cells to normalize single-cell rna sequencing data with many zero counts. *Genome biology*, 17(1):1–14, 2016.

A. Lyubimova, S. Itzkovitz, J. P. Junker, Z. P. Fan, X. Wu, and A. Van Oudenaarden. Single-molecule mrna detection and counting in mammalian tissue. *Nature protocols*, 8 (9):1743, 2013.

K. R. Maynard, L. Collado-Torres, L. M. Weber, C. Uytingco, B. K. Barry, S. R. Williams, J. L. Catallini, M. N. Tran, Z. Besich, M. Tippani, et al. Transcriptome-scale spatial gene expression in the human dorsolateral prefrontal cortex. *Nature Neuroscience*, pages 1–12, 2021.

D. J. McCarthy, K. R. Campbell, A. T. Lun, and Q. F. Wills. Scater: pre-processing, quality control, normalization and visualization of single-cell rna-seq data in r. *Bioinformatics*, 33(8):1179–1186, 2017.

L. McInnes, J. Healy, and J. Melville. Umap: Uniform manifold approximation and projection for dimension reduction. *arXiv preprint arXiv:1802.03426*, 2018.

S. Mills. *Histology for pathologists*. Lippincott Williams & Wilkins, 2019.

P. Qiu. Embracing the dropouts in single-cell rna-seq analysis. *Nature communications*, 11 (1):1–9, 2020.

W. M. Rand. Objective criteria for the evaluation of clustering methods. *Journal of the American Statistical association*, 66(336):846–850, 1971.

S. G. Rodriques, R. R. Stickels, A. Goeva, C. A. Martin, E. Murray, C. R. Vanderburg, J. Welch, L. M. Chen, F. Chen, and E. Z. Macosko. Slide-seq: A scalable technology for measuring genome-wide expression at high spatial resolution. *Science*, 363(6434):1463–1467, 2019.

H. Schütze, C. D. Manning, and P. Raghavan. *Introduction to information retrieval*, volume 39. Cambridge University Press Cambridge, 2008.

S. Shah, E. Lubeck, W. Zhou, and L. Cai. In situ transcription profiling of single cells reveals spatial organization of cells in the mouse hippocampus. *Neuron*, 92(2):342–357, 2016.

P. L. Ståhl, F. Salmén, S. Vickovic, A. Lundmark, J. F. Navarro, J. Magnusson, S. Giacomello, M. Asp, J. O. Westholm, M. Huss, et al. Visualization and analysis of gene expression in tissue sections by spatial transcriptomics. *Science*, 353(6294):78–82, 2016.

V. Svensson. Droplet scrna-seq is not zero-inflated. *Nature Biotechnology*, 38(2):147–150, 2020.

V. A. Tolpekin and A. Stein. Quantification of the effects of land-cover-class spectral separability on the accuracy of markov-random-field-based superresolution mapping. *IEEE transactions on geoscience and remote sensing*, 47(9):3283–3297, 2009.

L. Van der Maaten and G. Hinton. Visualizing data using t-sne. *Journal of machine learning research*, 9(11), 2008.

T. N. Vu, Q. F. Wills, K. R. Kalari, N. Niu, L. Wang, M. Rantalainen, and Y. Pawitan. Beta-poisson model for single-cell rna-seq data analyses. *Bioinformatics*, 32(14):2128–2135, 2016.

L. N. Waylen, H. T. Nim, L. G. Martelotto, and M. Ramialison. From whole-mount to single-cell spatial assessment of gene expression in 3d. *Communications biology*, 3(1):1–11, 2020.

C. Xia, H. P. Babcock, J. R. Moffitt, and X. Zhuang. Multiplexed detection of rna using merfish and branched dna amplification. *Scientific reports*, 9(1):1–13, 2019.

Y. Zhang, M. Brady, and S. Smith. Segmentation of brain mr images through a hidden markov random field model and the expectation-maximization algorithm. *IEEE transactions on medical imaging*, 20(1):45–57, 2001.

E. Zhao, M. R. Stone, X. Ren, J. Guenthoer, K. S. Smythe, T. Pulliam, S. R. Williams, C. R. Uytingco, S. E. Taylor, P. Nghiem, et al. Spatial transcriptomics at subspot resolution with bayesspace. *Nature Biotechnology*, pages 1–10, 2021.

Q. Zhu, S. Shah, R. Dries, L. Cai, and G.-C. Yuan. Identification of spatially associated subpopulations by combining scrnaseq and sequential fluorescence in situ hybridization data. *Nature biotechnology*, 36(12):1183–1190, 2018.

Supplementary: SC-MEB: spatial clustering with hidden Markov random field using empirical Bayes

1 SC-MEB Method

1.1 the Hidden Markov random field model

Let $\mathcal{S}$ be the set of all spots with a neighborhood system defined on it. The cell types in each spot can be modeled by a hidden random field

$$\{x = (x_1, \ldots, x_N) \mid x_i \in \mathcal{L}, i \in \mathcal{S}\},$$

where N is the number of spots, and $\mathcal{L} = \{1, \ldots, K\}$ is the set of all possible cell types. The p-dimensional representation of the gene expression is modeled by an observed random field

$$\{y = (y_1, \ldots, y_N) \mid y_i \in \mathbb{R}^p, i \in \mathcal{S}\}.$$

For spot i, its neighbors we considered are the spots surrounding it, and is denoted by $\mathcal{N}_i$.

The representation of the gene expression y is assumed to be a Gaussian MRF model, with two prefixed parameters, the number of cell types K, and the smoothing parameter $\beta(> 0)$. Specifically, the observed random field y are assumed to be mutually independent given the hidden random field x, and normally distributed with:

$$p(y \mid x, \theta) = \prod_{i \in \mathcal{S}} \mathcal{N}(y_i | x_i = k, \mu_k, \Sigma_k),$$

where $\theta = \{\mu_k, \Sigma_k : k = 1, \ldots, K\}$, μ_k and Σ_k denote the mean and Covariance matrix for cell type k. The hidden random field x are assumed to be the Potts model:

$$\begin{aligned} P(x) &= \frac{1}{Z_\beta} \exp\{-U(x)\}, \\ U(x) &= \sum_{i, i' \in \mathcal{N}_i} \beta[1 - \delta(x_i, x_i')], \end{aligned} \tag{1}$$

where δ is the delta function, and Z_β is a normalization constant that lacks a closed form.

With prefixed (K, β), the question of interest is to recover the unknown cell types x, interpreted as a clustering into a finite number K of types. This clustering usually is conducted based on the posterior distribution of x, and requires the estimation of parameter θ.

1.2 ICM-EM algorithm

Estimation of the parameter is done using an iterative conditional mode based expectation-maximization (ICM-EM) algorithm [Cuadra et al., 2005]. We assume (K, β) is known at present, and will discuss their selection in next section.

In ICM step, the estimate of x is obtained by maximizing its posterior with respect to x_i coordinately:

$$P(x \mid y) = P(x_i, x_{\mathcal{S}-\{i\}} \mid y) = P(x_i \mid y, x_{\mathcal{S}-\{i\}}) P(x_{\mathcal{S}-\{i\}} \mid y),$$

where $i = 1, \ldots, n$, until converge [Besag, 1986]. Given initial values of x, θ, and observed y, we have the update equation:

$$\hat{x}_i = \min_{x_i} U(\hat{x}_1, \ldots, x_i, \ldots, \hat{x}_n), \tag{2}$$

where

$$\begin{aligned} U(x) = & \Big\{ \frac{1}{2}(y_i - \mu_{x_i})^\top \Sigma_{x_i}^{-1} (y_i - \mu_{x_i}) + \frac{1}{2} \log |\Sigma_{x_i}| \\ & + \beta \sum_{i' \in \mathcal{N}_i} [1 - \delta(x_i, x_{i'})] \Big\}. \end{aligned}$$

In EM step, instead of the original complete likelihood which is difficult to perform the E-step, the following pseudo-likelihood is used:

$$\begin{aligned} \tilde{p}(y, x; \theta) &= p(y|x; \theta) \tilde{p}(x; \theta) \\ &= \prod_i p(y_i \mid x_i; \theta) \prod p(x_i | x_{\mathcal{N}_i}; \theta) \\ &= \prod_i [p(y_i \mid x_i; \theta) p(x_i | x_{\mathcal{N}_i}; \theta)] \\ &= \prod_i p(y_i, x_i \mid x_{\mathcal{N}_i}; \theta). \end{aligned}$$

For any $q_i(x_i)$, we have

$$\begin{aligned}
\log \tilde{p}(y;\theta) &= \sum_i \log \sum_k p(y_i, x_i = k \mid x_{\mathcal{N}_i};\theta) \\
&= \sum_i \log \sum_k q_i(x_i = k) \frac{p(y_i, x_i = k \mid x_{\mathcal{N}_i};\theta)}{q_i(x_i = k)} \\
&= \sum_i \log \mathbf{E}_{x_i} \left[\frac{p(y_i, x_i \mid x_{\mathcal{N}_i};\theta)}{q_i(x_i)} \right] \\
&\geq \sum_i \mathbf{E}_{x_i} \left[\log \frac{p(y_i, x_i \mid x_{\mathcal{N}_i};\theta)}{q_i(x_i)} \right] := \mathrm{ELBO}(\theta).
\end{aligned}$$

The above inequality is an equality if and only if

$$q_i(x_i) = \frac{p(y_i, x_i \mid x_{\mathcal{N}_i};\theta)}{\sum_{x_i} p(y_i, x_i \mid x_{\mathcal{N}_i};\theta)} = p(x_i \mid y_i, x_{\mathcal{N}_i}).$$

Then we have

$$\begin{aligned}
\mathrm{ELBO}(\theta) =& \sum_i \sum_k \gamma_{ik} \log p(y_i, x_i = k \mid x_{\mathcal{N}_i};\theta) - \sum_i \sum_k \gamma_{ik} \log \gamma_{ik} \\
=& \sum_i \sum_k \gamma_{ik} \left[\log p(y_i \mid x_i = k;\theta) + \log p(x_i = k \mid x_{\mathcal{N}_i};\theta) \right] \\
& - \sum_i \sum_k \gamma_{ik} \log \gamma_{ik}, \\
:=& Q(\theta) + \mathrm{Const},
\end{aligned}$$

where γ_{ik} is called responsibility that component k takes for explaining the observation y_i, and is defined as follows:

$$\gamma_{ik} = \frac{P(y_i \mid x_i = k) P(x_i = k \mid X_{\mathcal{N}_i} = \hat{x}_{\mathcal{N}_i})}{\sum_{k'} P(y_i \mid x_i = k') P(X_i = k' \mid X_{\mathcal{N}_i} = \hat{x}_{\mathcal{N}_i})}. \tag{3}$$

By taking partial derivatives of $\mathrm{ELBO}(\theta)$ with respect to the parameters and setting them to zero, we obtain the update equations for the maximization step:

$$\mu_k = \frac{1}{N_k} \sum_{i=1}^{n} \gamma_{ik} y_i, \tag{4}$$

$$\Sigma_k = \frac{1}{N_k} \sum_{i=1}^{n} \gamma_{ik} (y_i - \mu_k)(y_i - \mu_k)^\top. \tag{5}$$

where $N_k = \sum_{i=1}^{n} \gamma_{ik}$.

The ICM-EM algorithm iterates the ICM step and maximization steps until convergence. Implementations are summarized in Algorithm 1 for clarity.

Algorithm 1: ICM-EM with prefixed (K, β)

Initialize $x, \theta = \{\mu_k, \Sigma_k : k = 1, \ldots, K\}$.
repeat
  ICM-step:
  while *the change of* $U(x)$ *is larger than a threshold* **do**
    for $i = 1, \ldots, n$ **do**
      $\hat{x}_i = \min_{x_i} U(\hat{x}_1, \ldots, x_i, \ldots, \hat{x}_n)$, ;
    end
  end
  E-step:
  for $i = 1, \ldots, n, k = 1, \ldots, K$ **do**
    $\gamma_{ik} = \frac{P(y_i|x_i=k)P(x_i=k|X_{\mathcal{N}_i}=\hat{x}_{\mathcal{N}_i})}{\sum_{k'} P(y_i|x_i=k')P(X_i=k'|X_{\mathcal{N}_i}=\hat{x}_{\mathcal{N}_i})}$;
  end
  M-step:
  for $k = 1, \ldots, K$ **do**
    $N_k = \sum_{i=1}^{n} \gamma_{ik}$;
    $\mu_k = \frac{1}{N_k} \sum_{i=1}^{n} \gamma_{ik} y_i$;
    $\Sigma_k = \frac{1}{N_k} \sum_{i=1}^{n} \gamma_{ik}(y_i - \mu_k)(y_i - \mu_k)^\top$;
  end
until *the change of* $\log \tilde{p}(y; \theta)$ *is smaller than a threshold*;
return $\hat{x}$ *and* θ.

1.3 Spatial clustering model selection with BIC

Since the number of cell types and the smoothing parameter β are not known in advance, we use the Bayesian Information Criterion (BIC) to choose them.

Let M_r denote a MRF model with prefixed (K_r, β_r), where $K_r = K_{\min}$ to $K_r = K_{\max}$, and $\beta_r \in \{2^{-2}, 2^{-1}, \ldots, 2^4\}$. Denote θ_r the parameters in M_r. BIC is defined as follows:

$$\mathrm{BIC}(\hat{\theta}_r) = 2 \log p(y \mid \hat{\theta}_r) - d_r \log n, \tag{6}$$

where d_r the number of free parameters in M_r, and equals to $K \times p + K \times \frac{p(p+1)}{2}$ in a K-labels MRF model. Here the logarithm of the observed likelihood $p(y \mid \hat{\theta}_r)$ is approximated with the $\log \tilde{p}(y; \hat{\theta}_r)$.

2 Simulation Results

2.1 Additional results for Example I

In Example I, lables of spots are radomly generated. We generated 4900 spatial spots defined on a 70×70 square lattices, and simulated the cluster label for each spot from the K-states Potts model with $\beta \in [1, 1.3]$ using the R package *GiRaF*. The number of neighbors is set to 4 and the number of true clusters K is set to be 3, 5 or 7. At last, two distributions are considered for PC representations of gene expression: a Gaussian mixture model, and a Student-t mixture model. The number of PCs was set to be either 10, or 15. The component mean μ_k and the component covariance matrix Σ_k are described in Supplementary Table S1-S4.

Figure S1. All component densities have different covariances, and the number of PCs was set to be 10.

Figure S2. All component densities have different covariances, and the number of PCs was set to be 15.

Figure S3. All components have a shared covariance, and the number of PCs was set to be 10.

Figure S4. All components have a shared covariance, and the number of PCs was set to be 15.

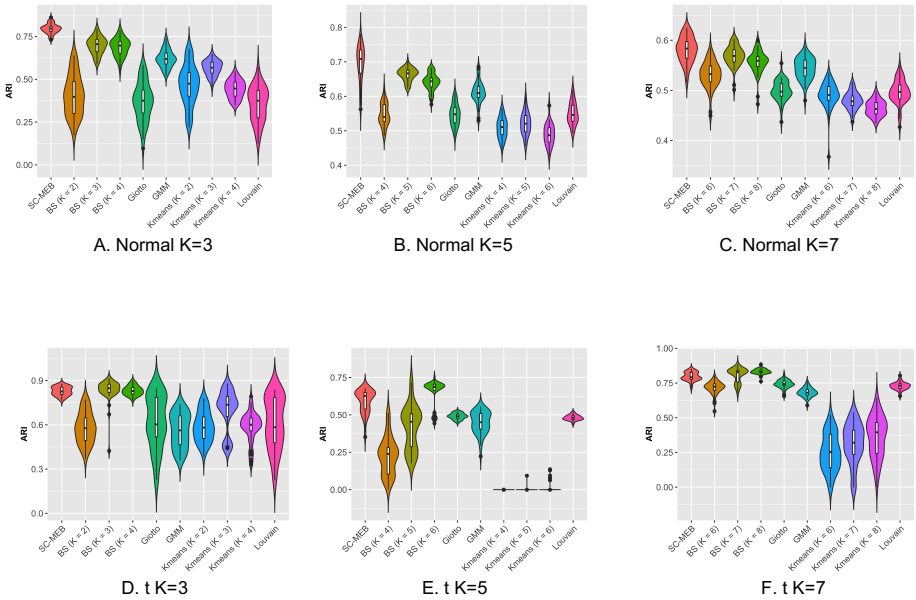

Figure S1: Additional results for Example I. All component densities have different covariances, and the number of PCs was set to be 10. **A-C.** PCs are sampled from a Gaussian mixture model, and the number of true clusters K is set to be be 3, 5 or 7. **D-F.** PCs are sampled from a Student-t mixture model, and the number of true clusters K is set to be be 3, 5 or 7.

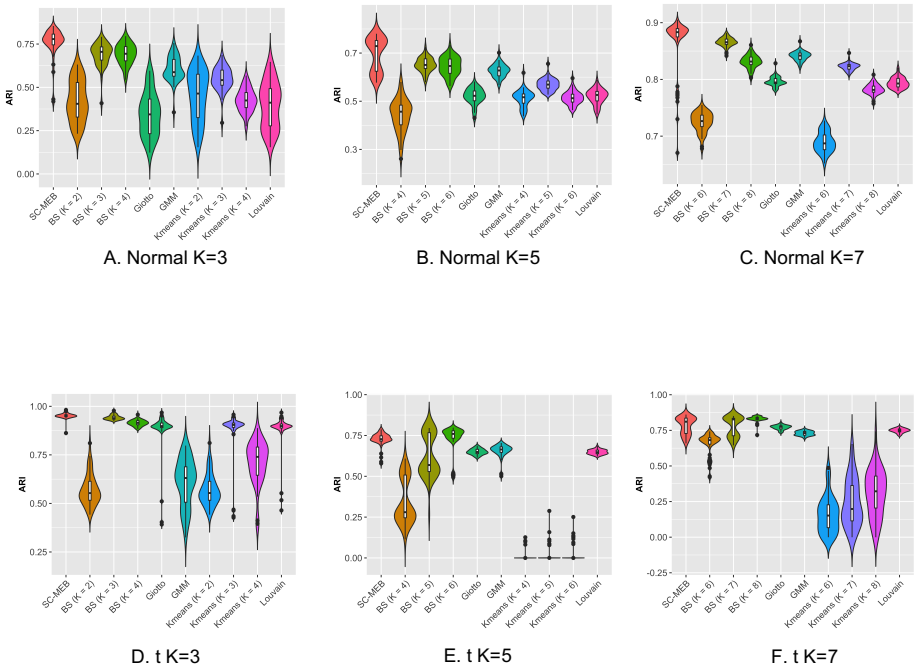

Figure S2: Additional results for Example I. All component densities have different covariances, and the number of PCs was set to be 15. **A-C.** PCs are sampled from a Gaussian mixture model, and the number of true clusters K is set to be be 3, 5 or 7. **D-F.** PCs are sampled from a Student-t mixture model, and the number of true clusters K is set to be be 3, 5 or 7.

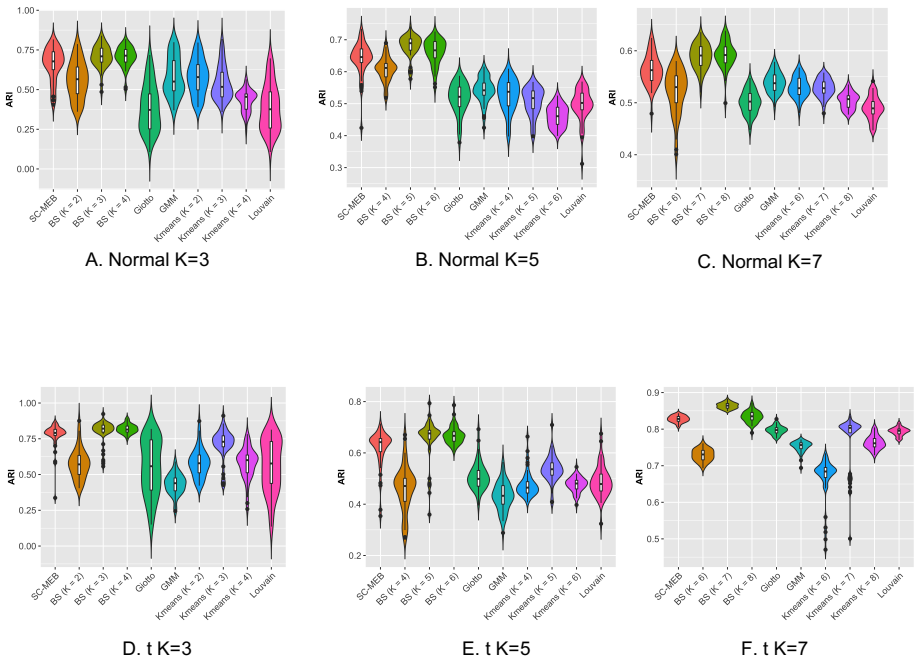

Figure S3: Additional results for Example I. All components have a shared covariance, and the number of PCs was set to be 10. **A-C.** PCs are sampled from a Gaussian mixture model, and the number of true clusters K is set to be be 3, 5 or 7. **D-F.** PCs are sampled from a Student-t mixture model, and the number of true clusters K is set to be be 3, 5 or 7.

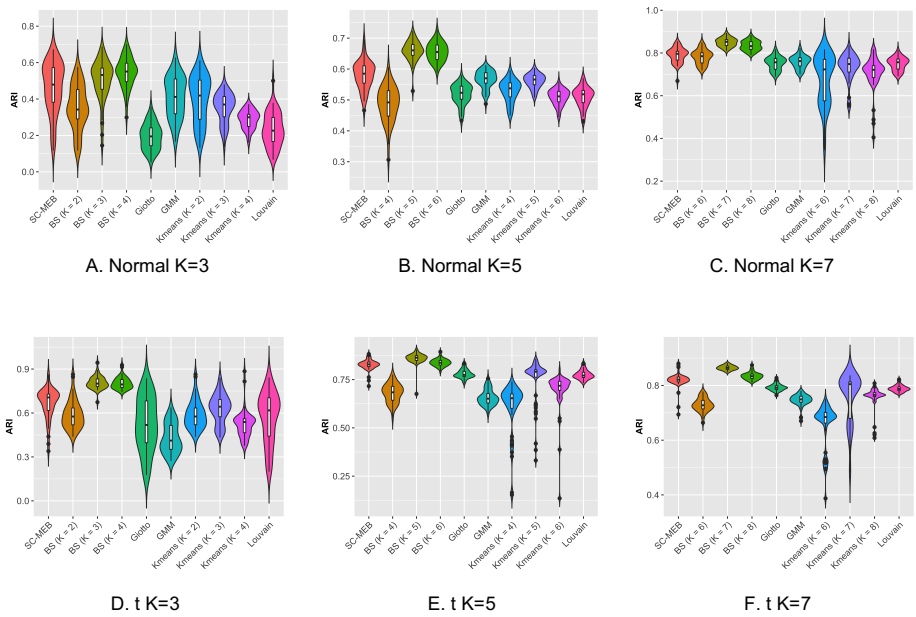

Figure S4: Additional results for Example I. All components have a shared covariance, and the number of PCs was set to be 15. **A-C.** PCs are sampled from a Gaussian mixture model, and the number of true clusters K is set to be be 3, 5 or 7. **D-F.** PCs are sampled from a Student-t mixture model, and the number of true clusters K is set to be be 3, 5 or 7.

2.2 Additional results for Example II

In Example II, lables of spots are obtained from our real data. Specifically, we obtained labels of 2,988 spots in the CRC data inferred from the corresponding real data with SC-MEB ($K = 8$). PCs were sampled in the same way as Example I. The component mean μ_k and the component covariance matrix Σ_k are described in Supplementary Table S5-S6.

Figure S5. The number of PCs was set to be 10.

Figure S5. The number of PCs was set to be 15.

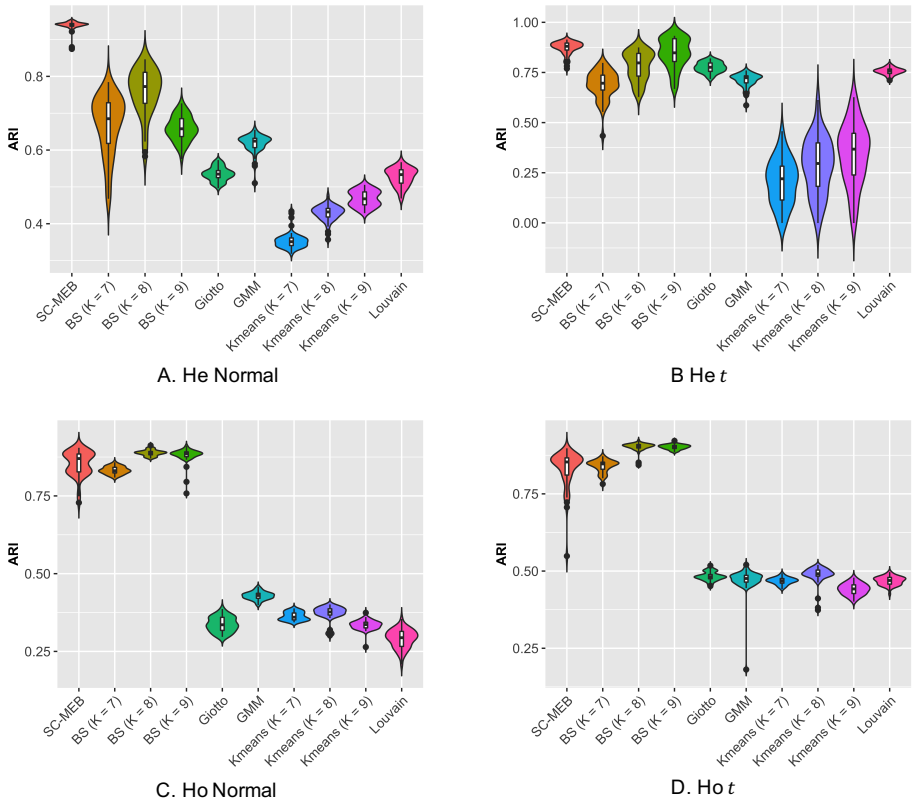

Figure S5: Additional results for Example II. The number of PCs was set to be 10. **A-B.** PCs are sampled from a Gaussian mixture model, and all component densities have different covariances. **C-D.** PCs are sampled from a Gaussian mixture model, and all components have a shared covariance.

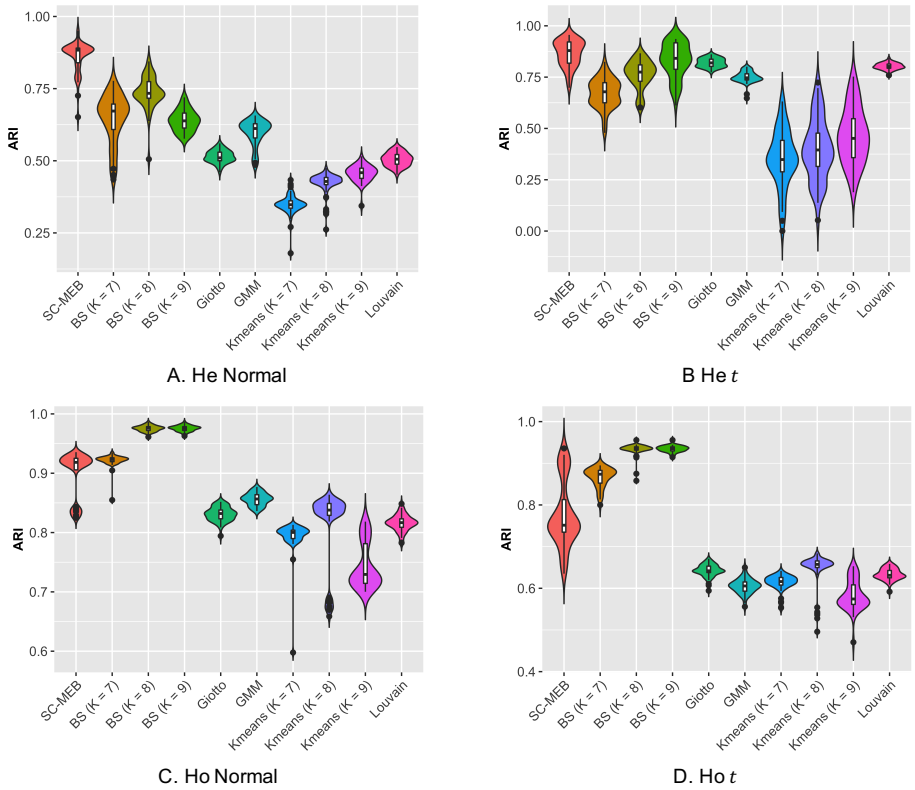

Figure S6: Additional results for Example II. The number of PCs was set to be 15. **A-B.** PCs are sampled from a Gaussian mixture model, and all component densities have different covariances. **C-D.** PCs are sampled from a Gaussian mixture model, and all components have a shared covariance.

References

Julian Besag. On the statistical analysis of dirty pictures. *Journal of the Royal Statistical Society: Series B (Methodological)*, 48(3):259–279, 1986.

Meritxell Bach Cuadra, Leila Cammoun, Torsten Butz, Olivier Cuisenaire, and J-P Thiran. Comparison and validation of tissue modelization and statistical classification methods in t1-weighted mr brain images. *IEEE transactions on medical imaging*, 24(12):1548–1565, 2005.